THE ASTROPHYSICAL JOURNAL, 386:229–238, 1992 February 10

WINDS FROM T TAURI STARS. II. BALMER LINE PROFILES FOR INNER DISK WINDS

NURIA CALVET
Centro de Investigaciones de Astronomia, Ap. Postal 264, Mérida 5101-A, Venezuela
AND
LEE HARTMANN AND ROBERT HEWETT
Harvard-Smithsonian Center for Astrophysics, Mail Stop 15, 60 Garden Street, Cambridge, MA 02138
Received 1991 June 3; accepted 1991 August 13

ABSTRACT

Balmer line profiles have been calculated using escape probability methods for T Tauri wind models with non–spherically symmetric geometry. The wind is assumed to originate in the inner regions of an accretion disk surrounding the T Tauri star, and flows outward in a "cone" geometry. We consider two types of wind models, both with monotonically increasing expansion velocities as a function of radial distance. For flows with large turbulent velocities, such as the high-frequency Alfvén wave-driven wind models, the effect of cone geometry is to increase the blue wing emission, and to move the absorption reversal close to line center. This type of model can provide good agreement with observed Hα line profiles of some T Tauri stars. However, even in cone geometry turbulent wind models still tend to produce too much blueshifted absorption in Hβ and Hγ. We have also calculated line profiles for a wind model rotating with the same angular velocity as the inner disk. The Balmer lines of this model are significantly broader than observed in most objects, suggesting that the observed emission lines do not arise in a region rotating at Keplerian velocity. Both turbulent and rotating wind models have difficulties explaining the centrally peaked emission line profiles often observed. Thus, the wind models considered here do not provide very satisfactory explanations of the Balmer line profiles of many T Tauri stars.

Subject headings: line: formation — line: profiles — stars: emission-line, Be — stars: mass-loss — stars: pre–main-sequence

1. INTRODUCTION

The broad emission lines of the low-mass, pre–main-sequence T Tauri stars are usually thought to arise in a wind (Kuhi 1964; Kuan 1975; DeCampli 1981; Hartmann, Edwards, & Avrett 1982; Lago 1979, 1984; Natta, Giovanardi, & Palla 1988; Natta & Giovanardi 1990; Hartmann et al. 1990, hereafter Paper I). Wind models have been relatively successful in explaining the hydrogen and low-excitation metal emission-line strengths, and provide a general framework to explain the blueshifted absorption frequently seen in strong lines (e.g., Herbig 1977). However, the calculated line profiles often fail to reproduce the observations very well. Many T Tauri stars exhibit Balmer emission lines that are broad and nearly symmetric, with relatively small velocities for the blueshifted absorption component. In contrast, accelerating wind models tend to produce highly asymmetric profiles, and high-velocity blueshifted absorption. Wind models with large "turbulent" velocities show somewhat better agreement with observations (Hartmann 1986) but are not entirely successful (Paper I). The profiles of decelerating wind models have small blueshifts of the absorption components (Grinin & Mitskevich 1991), but constructing hydrodynamic wind models with asymptotic velocities well below the surface escape velocity is difficult (Holzer, Fla, & Leer 1983).

Most attempts to model the permitted line profiles of T Tauri winds have assumed a stellar origin for the mass outflow, and thus adopt spherically symmetric geometry for simplicity. However, it has become clear in recent years that the stellar wind theory has grave difficulties. Current stellar wind theories invoke magnetohydrodynamic waves to drive the flow, with energy fluxes $\gtrsim 10^{-1}$ of the stellar luminosity (DeCampli 1981; Hartmann et al. 1982, hereafter HEA; Lago 1979, 1984), and the ability of the star to generate such large MHD wave energy fluxes is questionable (Calvet & Albarrán 1984).

The emission activity of T Tauri stars is now thought to be powered by mass accretion from circumstellar disks (Lynden-Bell & Pringle 1974; Bertout 1987; Kenyon & Hartmann 1987; Bertout, Basri, & Bouvier 1988; Basri & Bertout 1989). Disk accretion can in principle provide the energy for T Tauri winds (Pudritz & Norman 1983; Pringle 1989; Königl 1989). The observed strengths of the optical emission lines are correlated with the presence of excess infrared and ultraviolet continuum fluxes attributed to the accretion disk and the boundary layer, respectively (Cohen, Emerson, & Beichman 1989; Cabrit et al. 1990; Hartigan et al. 1990). Line profiles for T Tauri disk winds could differ qualitatively from the profiles calculated for stellar wind models, because the disk winds would not be spherically symmetric. Moreover, because the disk is in Keplerian rotation, a wind from the inner disk would exhibit large rotational velocities, in contrast to the stellar wind case.

In this paper we compute Balmer line profiles for monotonically expanding winds which have the qualitative features expected for flows from the innermost disk or boundary layer. We find that geometry and rotational velocities have important qualitative effects on the line shapes. However, these models still have difficulties in explaining the centrally peaked emission seen in many objects, and the calculated Hβ and Hγ profiles tend to be too asymmetric. The observed line widths also place stringent constraints on the magnitude of any possible rotational velocity field.

2. CALCULATIONS

2.1. *Wind Geometry*

We assume that the wind originates in the inner disk or in the boundary-layer between the slowly rotating star and the rapidly rotating disk. Our choice is motivated by the large rotational velocities expected in the inner disk, which may be responsible for the acceleration of the wind (Blandford & Payne 1982; Pudritz & Norman 1983). In addition, the boundary layer may have large turbulent velocities and may generate large fluxes of high-frequency MHD waves, which could also help drive and heat the wind (Pringle 1989). Wind models with similar conical geometry have also been developed to explain the profiles of the optically thin forbidden emission lines observed in some T Tauri stars (Edwards et al. 1987).

We take a coordinate system (x, y, z) centered on the star, with the z-axis directed toward the observer, and a coordinate system (x', y', z'), which corresponds to a rotation of the first system by an angle i around the axis $x = x'$. The disk is located on the plane (x', y') of coordinate system (x', y', z'), so that the angle i between the z and z' axes is the inclination of the system star + disk to the line of sight. Because the wind arises in the inner disk or boundary layer, we assume that the flowing material occupies a conelike geometry, with axis of symmetry equal to the z' coordinate (see Fig. 1). The matter is assumed to flow out from the (x', y') plane on the circle $x'^2 + y'^2 = R_*^2$, where R_* is the stellar radius. It occupies the region between angles θ_1 and θ_2, where θ is the angle to the normal to the disk on this circle (see Fig. 1).

The wind expands with a velocity $\boldsymbol{v}$ in the direction of the vector $\boldsymbol{r}_*$, which joins a point in the cone to the stellar equator. The magnitude of $\boldsymbol{v}$ depends only on r_*. The cone extends to the maximum radius of the region, r_{max}. We also consider one rotating wind model, which has an azimuthal velocity component in the (x', y') plane, in the direction of the spherical coordinate ϕ. The angular velocity is arbitrarily assumed to be constant out to a radial distance from the center of the star $r = 2.5R_*$, after which the azimuthal velocity decreases as r^{-1}.

The broadening velocity is included as a microturbulent contribution to the Doppler width. We use a tangential broadening in the wave-driven wind calculations, that is, a broadening perpendicular to the direction of $\boldsymbol{r}_*$, to simulate the broadening due to high-frequency Alfvén waves (see Paper I).

2.2. *Radiative Transfer Solutions*

We solve the transfer equation for the specific intensity I_ν at frequency ν along rays specified by constant values of x and y:

$$\frac{dI_\nu}{dz} = \eta_\nu - \chi_\nu I_\nu , \tag{1}$$

where η_ν and χ_ν are the emission and absorption coefficients at frequency ν and point specified by coordinates (x, y, z). These coefficients are a function of r_* and θ inside the cone, and are zero outside it. Once the specific intensity I_ν is known for each ray (x, y), the flux at frequency ν in the line is calculated by direct integration over the emitting area.

In view of our ignorance of the detailed temperature and density structure of T Tauri winds, we adopt approximate methods to compute the line optical depths and source functions. Ion and electron densities for the given temperature and total hydrogen density at each radius are calculated assuming spherical symmetry with the PANDORA radiative transfer code (Avrett & Loeser 1984; see also Paper I). The $n = 1$–4 level populations from the spherically symmetric results are used to calculate line and continuum opacities and line escape probabilities for a given geometry, as described below. Given these escape probabilities, which depend on the location (r_* and θ) inside the cone, we calculate line source functions by solving the statistical equilibrium equations for an eight-level hydrogen atom. The $n = 1$ level populations are assumed fixed,

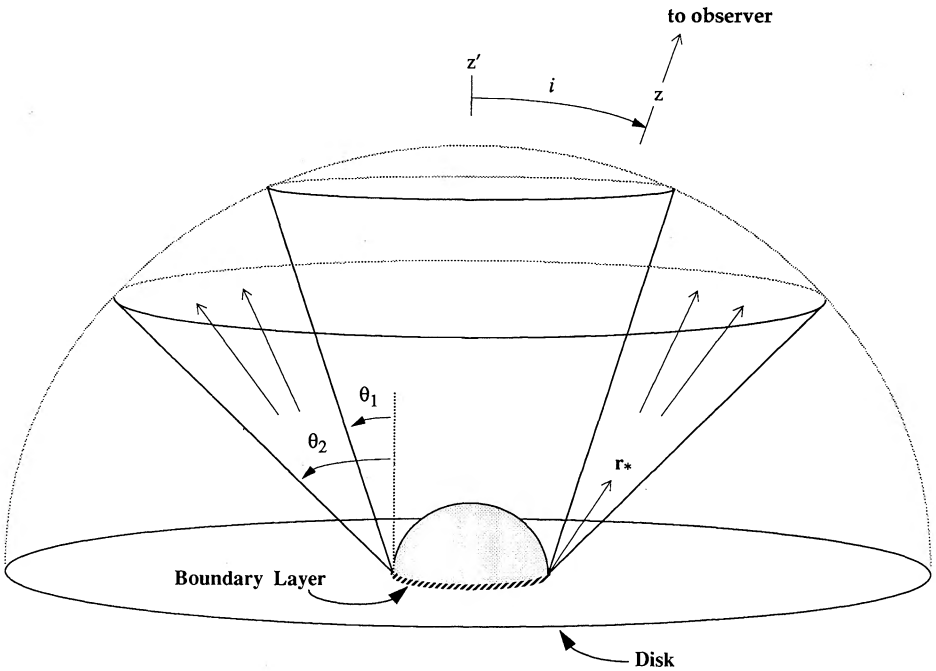

FIG. 1.—Schematic depiction of adopted geometry. The wind is assumed to flow in a cone between the angles θ_1 and θ_2, and the observer's line of sight makes an angle i with respect to the polar axis. The disk is assumed to be optically thick and obscures all emission from the far side.

with the net radiative brackets for Lyα, Hα, Hβ, Hγ, Pα, Pβ, and Brα set equal to the corresponding escape probabilities. The escape probabilities for all Lyman lines are assumed to be equal to that of Lyα. The other radiative transitions for the eight-level atom are assumed to be optically thin. The continuum rates are calculated with a fixed radiation temperature of 4500 K for $n \geq 2$.

The solution of the statistical equilibrium equations results in different populations for $n \geq 2$ than were used to calculate the Balmer line optical depths and hence the escape probabilities. In practice the $n = 2$ populations do not change greatly, because they are mostly controlled by escape in the Lyα line. This line is so optically thick that it is nearly thermalized in these models, resulting in departure coefficients $b_2 \sim b_1$. Only near the very edge of the cone does the Lyα line become effectively thin, and the $n = 2$ level population becomes geometry-dependent. Our method should be most accurate for fairly wide cones; in the limit $\theta_2 - \theta_1 \rightarrow \pi/2$ we recover the detailed PANDORA spherically symmetric results at the middle of the cone.

Our approach permits an initial exploration of the *qualitative* effects of non–spherically symmetric geometry on the profiles of optically thick lines, but quantitative details should be regarded with caution. Ultimately, the escape probabilities should be iterated with the statistical equilibrium equations to provide a self-consistent solution, but this approach requires a very time-consuming calculation, since the escape probabilities must be computed at many more spatial locations than in a spherically symmetric model. We feel that our approximate procedure is justified since the detailed temperature structure of the wind is not well-constrained by either theory or observation.

The escape probability is defined as (Mihalas 1978)

$$\rho(\mathbf{r}) \sim \frac{1}{2\pi} \int d\Omega \int_{-\infty}^{\infty} \phi(x) e^{-\tau_x} dx \,, \tag{2}$$

where $d\Omega$ is the element of solid angle and τ_x and ϕ_x are the optical depth and profile function at frequency x. We assume for simplicity that azimuthal symmetry holds, that is, $d\Omega = 2\pi\, d\mu$, where $\mu = \cos(\theta)$, although it is not appropriate in our case. This assumption implies that the escape in all directions in the cone is the same as that in the plane defined by vectors $\hat{z}'$, $\mathbf{r}_*$. Since the photons most freely escape in this plane, the calculated escape probability will be an upper limit to the true escape probability.

The optical depth τ_x, in the case of a uniform sphere expanding with velocity proportional to the distance, is given by (Capriotti 1965)

$$\tau_x = \tau_0 (v_{\rm th}/v_e) \int_{x - v_e/v_{\rm th}}^{x} \phi(y) dy \,, \tag{3}$$

where $v_{\rm th}$ is the broadening velocity, with thermal and "turbulent" contributions, v_e is the expansion velocity at the surface (relative to the point where the photons are emitted), and τ_0 is the optical depth in the static case. For a Voigt profile, $\phi(x) \sim a/\pi x^2$, where a is the damping parameter, the optical depth is

$$\tau_x = \frac{a\tau_0}{\pi} \frac{1}{[x(x - v_e/v_{\rm th})]} \,. \tag{4}$$

The escape probability is given by

$$\rho(\mathbf{r}) \sim \tfrac{1}{2} \int d\mu \left[\int_{-\infty}^{x_1} \phi(x) dx + \int_{x_2}^{\infty} \phi(x) dx \right] , \tag{5}$$

where x_1 and x_2 are the frequencies where $\tau_x = 1$. Here we have used the approximations $e^{-\tau_x} \sim 0$ if $x_1 < x < x_2$, and $e^{-\tau_x} \sim 1$ otherwise. For a Voigt profile, the escape probability is given by

$$\rho(\mathbf{r}) \sim \int d\mu [(v_e/v_{\rm th})^2 + 4a\tau_0/\pi]^{1/2}/2\tau_0 \,. \tag{6}$$

The net escape probability is thus a quadratic mean of a Sobolev expression (see Castor 1970) and the static escape probability, and asymptotically approaches the Sobolev limit for large values of $v_e/v_{\rm th}$. Thus, we are not limited to exploring wind models in which the Sobolev criterion is satisfied, but can also investigate winds with large "turbulent" velocities.

For a given type of profile, the escape probability is evaluated from equation (6) integrating over angles at a given point inside the cone specified by coordinates (r_*, θ), with a $n = 20$ Gaussian quadrature. Along the ray determined by each quadrature angle, the optical depth τ_0 is determined by direct integration along the ray, and the damping parameter is estimated by the mean over the ray. The parameter $v_e/v_{\rm th}$ is estimated by the mean over the ray of the quantity $v_{\rm rel}/v_{\rm th} = [v_s(r'_*) - v_s(r_*)]/v_{\rm th}(r_*)$, where v_s is the component along the ray of the expansion velocity at points r'_* (along the ray) and r_* (where the escape probability is evaluated).

3. RESULTS

The wind models adopted in this paper have characteristics similar to those of the spherically symmetric wind models of Paper I in the outer regions, so that the effects of geometry on the line profiles may be more clearly isolated. The wind densities and temperatures are similar to those of model 15 in Paper I, for $r_* \geq 1R_*$, and join smoothly to a region of high density and $T = 8000$ K for $r_* \leq 0.1R_*$ (Table 1), which is intended to mimic a hot, dense boundary layer. For an adopted cone geometry, i.e., angles θ_1 and θ_2, the mass-loss rate of the model is calculated at the outer radius, using a velocity equal to the velocity at the corresponding depth in the spherically symmetric models in Paper I (219 km s^{-1}). The magnitude of the velocity at each point in the cone is calculated from the adopted mass-loss rate and density structure using mass conservation for steady flow. For a given mass-loss rate and density distribution the expansion velocities are smaller in wider cones, in proportion to the cone areas $4\pi r_*[r_*(\cos\theta_1 - \cos\theta_2) - R_*(\theta_2 - \theta_1)]$.

3.1. *Turbulent Wind Models*

We initially consider a wind model in which mass is ejected from a nonrotating boundary layer with large turbulent velocities. This model is the analog of the Alfvén wave-driven stellar wind models (DeCampli 1981; HEA; Lago 1979, 1984), except that the boundary layer is envisaged as the only place where the required fluxes of Alfvén waves can be generated (see § 1). We adopt the same expansion and broadening velocities as in Paper I to most clearly isolate the effects of the cone geometry (see Table 1, Model 1). The adopted velocity structure is the result of a hydrodynamic calculation in spherical flow, and so is not strictly self-consistent with the adopted geometry. However, we have constructed Alfvén wave-driven

TABLE 1

WIND MODELS

r_*/R_*	T	n_H	n_e	$v_t(1)$	$v_e(1)$	$v_t(2)$	$v_e(2)$
10.48	5000.	1.79E+09	2.54E+06	10.0	219.0	10.0	110.0
9.04	5000.	2.37E+09	3.61E+06	10.0	218.0	10.0	109.0
8.09	5000.	2.93E+09	4.57E+06	10.0	217.0	10.0	108.5
6.89	5000.	3.95E+09	6.53E+06	10.0	216.0	10.0	108.0
5.89	5000.	5.28E+09	9.67E+06	12.0	215.0	10.0	107.5
4.88	5000.	7.42E+09	1.62E+07	19.0	214.0	10.0	107.0
3.90	5000.	1.11E+10	3.35E+07	30.0	213.0	10.0	106.4
3.50	5000.	1.34E+10	5.35E+07	36.0	212.0	10.0	106.0
3.10	5400.	1.66E+10	2.07E+08	42.0	210.0	10.0	105.0
2.50	6000.	2.45E+10	1.33E+09	54.0	203.0	20.0	101.5
1.91	6600.	4.08E+10	7.74E+09	67.0	188.0	30.0	94.0
1.31	7300.	8.63E+10	3.16E+10	80.0	158.0	40.0	79.0
1.12	8000.	1.17E+11	7.69E+10	82.0	147.0	50.0	73.5
0.938	9000.	1.70E+11	1.58E+11	85.0	129.0	60.0	64.5
0.742	9600.	2.85E+11	2.80E+11	86.0	107.0	70.0	53.5
0.569	10000.	5.03E+11	4.97E+11	84.0	85.3	80.0	42.7
0.450	10000.	8.58E+11	8.44E+11	82.0	67.4	82.0	33.7
0.400	10000.	1.13E+12	1.11E+12	80.0	59.4	80.0	29.7
0.360	10000.	1.43E+12	1.41E+12	78.0	53.1	78.0	26.6
0.310	10000.	2.02E+12	1.98E+12	76.0	45.0	76.0	22.5
0.270	10000.	2.66E+12	2.60E+12	74.0	40.0	74.0	20.0
0.190	10000.	6.11E+12	5.90E+12	68.0	26.0	68.0	13.0
0.110	8600.	2.22E+13	1.25E+13	58.0	13.0	58.0	6.5
0.070	8000.	6.66E+13	1.41E+13	50.0	7.0	50.0	3.5
0.030	8000.	3.72E+14	3.74E+13	40.0	3.0	40.0	1.5
0.0107	8000.	3.17E+15	1.17E+14	16.0	0.0	16.0	0.0
0.00679	8000.	5.01E+15	1.49E+14	11.0	0.0	11.0	0.0
0.00579	8000.	5.87E+15	1.62E+14	9.0	0.0	9.0	0.0
0.00479	8000.	7.10E+15	1.79E+14	7.9	0.0	7.9	0.0
0.00390	8000.	8.75E+15	2.00E+14	7.5	0.0	7.5	0.0
0.00290	8000.	1.18E+16	2.33E+14	6.6	0.0	6.6	0.0
0.00200	8000.	1.71E+16	2.82E+14	5.9	0.0	5.9	0.0
0.00160	8000.	2.14E+16	3.16E+14	4.7	0.0	4.7	0.0
0.00110	8000.	3.70E+16	4.16E+14	2.9	0.0	2.9	0.0
0.00078	8000.	7.70E+16	6.04E+14	0.0	0.0	0.0	0.0
0.00064	8000.	1.00E+17	6.89E+14	0.0	0.0	0.0	0.0
0.00045	8000.	1.30E+17	7.87E+14	0.0	0.0	0.0	0.0
0.0002	8000.	1.50E+17	8.47E+14	0.0	0.0	0.0	0.0
0.0000	8000.	1.60E+17	8.75E+14	0.0	0.0	0.0	0.0

NOTES.—r_*/R_* is the distance along the cone in units of the stellar radius; T is the temperature in K; n_H is the total hydrogen density; n_e is the electron density; $v_t(1)$ and $v_e(1)$ are the turbulent and expansion velocities, respectively, for the standard or high-velocity wind model, in km s^{-1}, and $v_t(2)$ and $v_e(2)$ are the corresponding quantities for the slow-velocity wind model.

wind models in cone geometry using the flux-tube approximation outlined in Hartmann & MacGregor (1982), and find similar expansion and turbulent velocities.

In Figure 2 we show the source function for Hα as a function of radial position evaluated at $\theta = 45°$ and $\theta = 30°$, which correspond to the cone center and wall, respectively, of this cone with $\theta_1 = 30°$, $\theta_2 = 60°$. The Hα line source function for the spherical case is also shown for comparison. Near the star, the source functions for the various cases agree, because the line optical depths are sufficient to ensure thermalization. Proceeding outwards, the source function of the cone decreases relative to the spherical case, due to the enhanced escape of radiation through the sides of the cone. The enhanced escape at the cone edge accounts for the lower line source function there. In the outermost regions, the cone line source functions become higher than in the spherical case. In these regions all lines, except the Lyman lines, are optically thin for any angular position in the cone, and in the eight-level H atom approximation, $n_3/n_2 \sim R_{k3}/A_{32}$ and $n_2/n_1 \sim R_{k2}/A_{21}\rho_{21}$, where R_{k2} and R_{k3} are the recombination rates to levels 2 and 3, A_{32} and

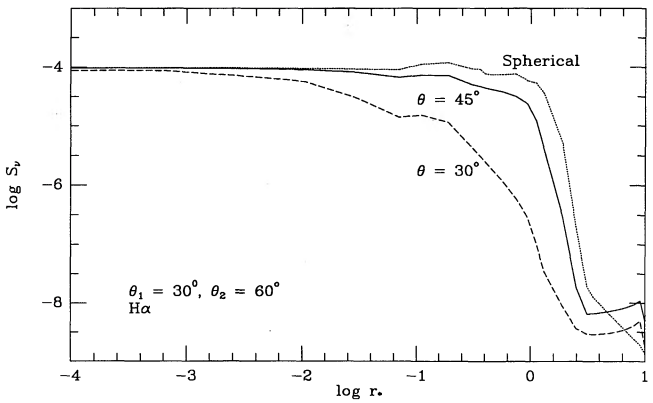

FIG. 2.—Hα line source functions for the standard wind model, flowing in a cone with $\theta_1 = 30°$ and $\theta_2 = 60°$. The dotted line denotes the PANDORA calculation for the spherically symmetric case. The solid line is the source function at $\theta = 45°$, i.e., at the midpoint of the cone flow; the dashed line shows the source function at the inner edge of the cone. The reduction in the source function due to increased escape of photons through the sides of the cone is evident. The turn-up of the source functions at large radii may be due to limitations of the escape probability methods, but in any event occur at small line optical depths and thus are not important for the line profiles, as discussed in the text. The small dip in the spherical line source function at $\log r_*/R_* = -0.4$ is due to a switch between the Sobolev escape probability and the static escape probability in the PANDORA calculations; the feature at $\log r_*/R_* \sim -1.2$ results from the way the wind was joined to the chromosphere.

A_{21} the Einstein coefficients of Hα and Lα, and ρ_{21} the escape probability of Lyα. The source function, which is proportional to n_3/n_2, reflects the decrease toward the surface of the population in the $n = 2$ level due to the increased escape in Lyα. A nebular approximation would be more appropriate in this case. In any event, since the Balmer lines are optically thin in these regions their contributions to the emergent fluxes are negligible.

Figure 3 exhibits line profiles for Hα, Hβ, and Hγ for this wind model. The leftmost panels show the line profiles calculated for the spherically symmetric case, with evident P Cygni structure (strong blueshifted absorption, prominent redshifted emission). The middle and right panels show the results for an adopted cone geometry $\theta_1 = 30°$, $\theta_2 = 60°$, viewed from inclination angles $i = 10°$, 30°, 60°, and 80°. The line fluxes for the cone case are reduced substantially due to the reduction of total mass-loss rate from the spherical case, and also because of the enhanced escape in the lines.

The net effect of the cone geometry is to move the blueshifted absorption to lower velocities when viewed at low inclinations. This effect results from the decline in the source functions near the edges of the cone, which produce low-velocity absorption from the inner regions of the wind, where expansion velocities are relatively small. At $i = 60°$, the observer's line of sight is along the cone, and so the extent of the blueshifted absorption is similar to that of the spherical case.

In Paper I we found that a reduction of the expansion velocities by a factor of 2, and a similar reduction in turbulent velocities, relative to the standard hydrodynamic model produced better agreement with observations of T Tauri stars. We present line profiles in Figure 4 for this "slow-velocity" model (Table 1), adopting a variety of opening angles (10°, 30°, 60°, 80°) for the cone flow. The same qualitative features discussed above for the standard wind case are also exhibited here, demonstrating that the precise opening angle adopted for the cone does not critically affect the line profiles.

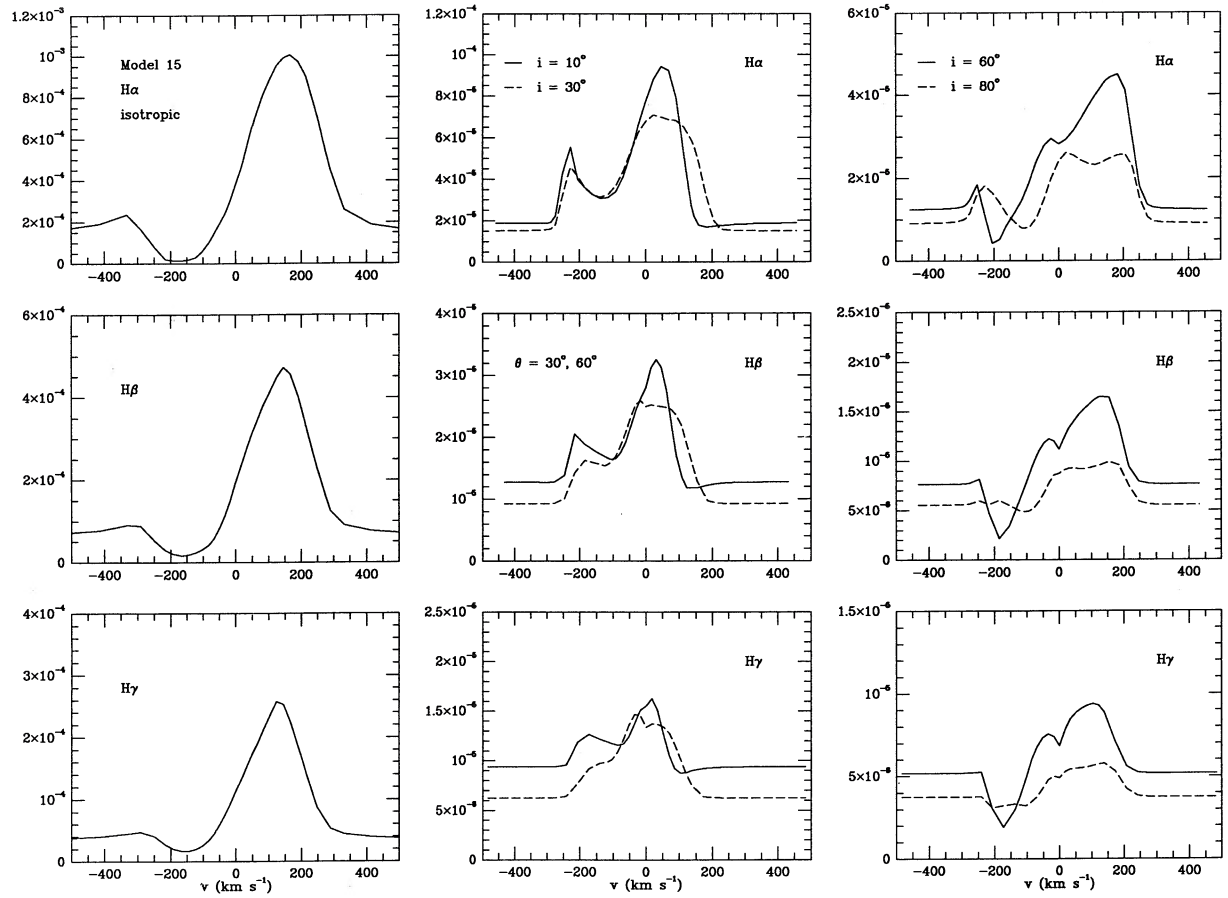

FIG. 3.—Line profiles for the standard wind model, based on model 15 of Paper I (see Table 1). The leftmost panels show the Hα, Hβ, and Hγ profiles for model 15 in spherical geometry. The other panels show the results for a cone wind with $\theta_1 = 30°$ and $\theta_2 = 60°$, observed at four values of the inclination angle i.

In both Figures 3 and 4, the centroids of the emission wings are blueshifted for $i = 10°$. This occurs because of occultation of the receding flow by the optically thick disk. At larger inclination angles, the far side of the observed cone (see Fig. 1) contributes more redshifted emission, and in combination with the large turbulent (symmetric) broadening velocity present in this wind model results in nearly centered emission wings.

3.2. *Wind Model with Rotation*

For the rotating wind case we adopt the same expansion velocities as in the slow model, but reduce the broadening velocities. We adopt the same turbulent broadening as in the slow wind model whenever $v_t \leq 40$ km s^{-1}, and use $v_t = 40$ km s^{-1} otherwise (see Table 1). In the absence of a detailed hydrodynamic calculation, we arbitrarily assume that the azimuthal velocity is given by solid body rotation out to $r = 2.5R_*$, beyond which it decreases inversely with increasing distance from the center.

Line profiles for the rotating wind model with a rotational velocity of 200 km s^{-1} at the base of the flow are shown in Figure 5. The profiles are "double-peaked" as expected. The line widths become large when viewed at inclinations $\geq 60°$. In our model, the maximum azimuthal velocity in the wind is $\sim$440 km s^{-1}. The profile widths are considerably narrower than this because the lines become optically thin relatively close to the stellar surface.

The emission from the rotating wind model is quite weak in comparison with the standard model. This results from the lower turbulent velocities adopted. Larger Hα equivalent widths, in better agreement with observations, could be obtained by increasing the turbulent velocity, or adopting a denser and/or hotter wind. (Note that for our assumption of solid-body rotation in the inner wind, the escape probabilities are not affected by the rotation. *Differential* rotation would increase the escape of photons in the same way as increasing the turbulent velocities.) Alternatively, for a given total mass-loss rate, a wind emanating from a disk annulus of finite area would have lower densities and higher escape probabilities, which could also increase the Hα equivalent width. We emphasize once again that our radiative transfer methods are approximate, and that the equivalent widths of the lines are uncertain, but the line shapes are likely to be indicative of the true solution.

4. DISCUSSION

In Figure 6 we display selected Hα line profiles of T Tauri stars for comparison with the wind model results. The spectra were obtained with the echelle spectrograph and intensified reticon detector on the 1.5 m telescope of the F. L. Whipple Observatory. The profiles shown in Figure 6 were chosen to cover the range of behavior observed. Additional Hα spectra were obtained with the KPNO 4 m echelle spectrograph in

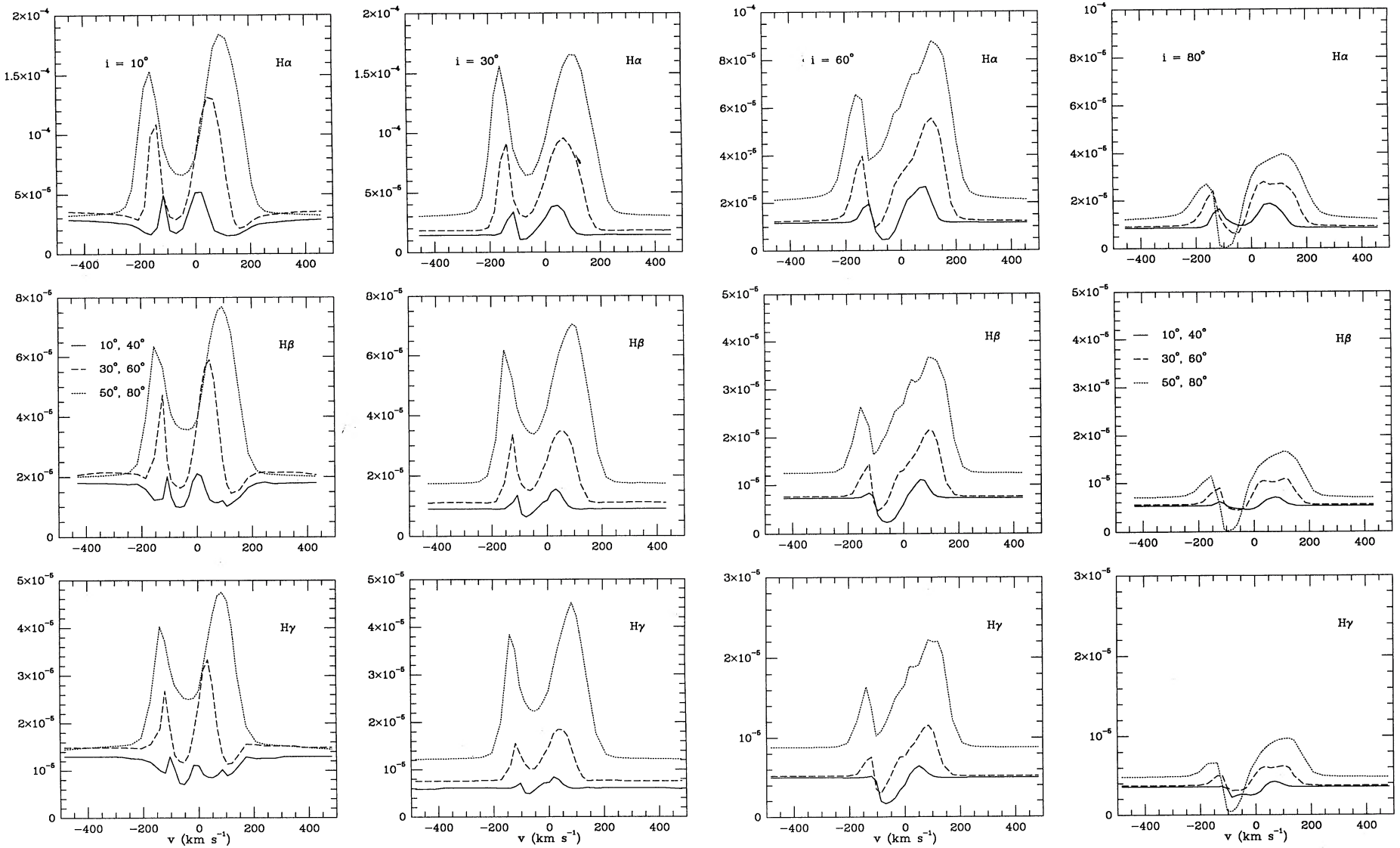

FIG. 4.—Line profiles for a wind model with the expansion and turbulent velocities reduced in half from model 15 (see Table 1). Calculations are shown for three pairs of θ_1, θ_2 values, as shown in the legend.

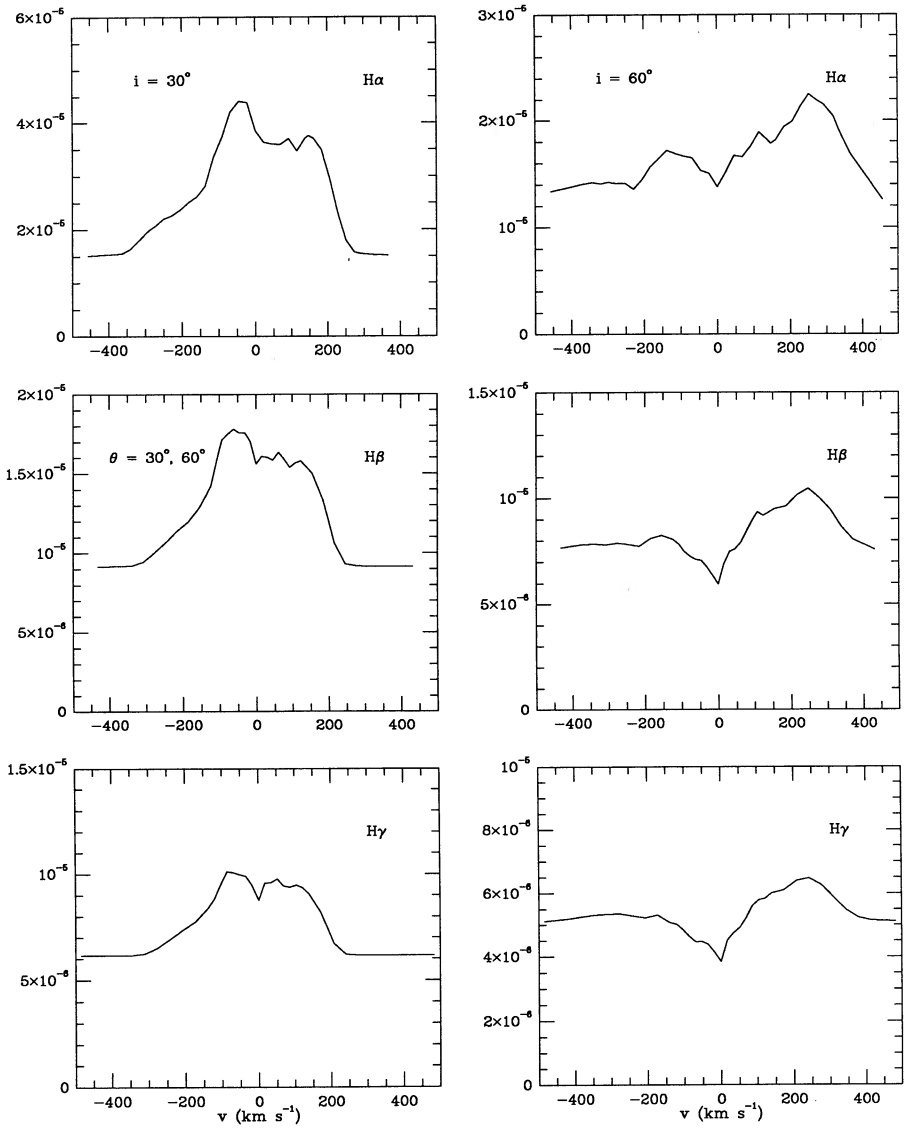

FIG. 5.—Line profiles for a rotating wind. The flow is assumed to have the same expansion velocity as the slow model (see Table 1). The turbulent velocities were taken to be equal to those of the slow model in Table 1 for $v_t \leq 40$ km s^{-1}, and otherwise $v_t = 40$ km s^{-1}. The rotational velocity at the base of the wind is 200 km s^{-1}, and the angular velocity is constant out to $r = 2.5R_*$, after which the azimuthal velocity decreases inversely with increasing distance from the center.

collaboration with John Stauffer, and the profiles will be published in another paper. In all, we have Hα profiles of 31 T Tauri stars in the Taurus-Auriga region which we use in the subsequent discussion for statistical purposes.

Comparison of the observed line profiles with the models suggests that the turbulent cone wind model can qualitatively explain the "central absorption" type of Hα line profile such as observed in AA Tau (Fig. 6). If we define a "central absorption" line profile to mean that the residual intensity at line center is less than half of the peak emission-line intensity, the data suggest that such profiles are seen in Hα ~ 10%–20% of the time. This is in approximate agreement with the models, which tend to show such absorption only when observed nearly pole-on. The agreement between models and observations is improved for the lower expansion velocity model. The turbulent, nonrotating wind model also can explain the nearly "classical" P Cygni line profiles observed in stars like DL Tau (Fig. 6), where the blueshifted absorption extends to comparable velocities as the blueshifted emission. The models predict strongly blueshifted absorption at inclination angles greater than about 45°, that is, about half of the time, which is roughly consistent with observations.

Present observations do not suggest any clear correlation between inclination and the presence of central absorption, as predicted by these models. For example, photometric and spectroscopic data suggest that DN Tau is nearly pole-on (Bouvier 1990; Basri & Bertout 1989), yet this object does not present centrally reversed Hα absorption. In addition, DF Tau may be observed nearly equator-on (Bertout, Basri, & Bouvier 1988; Basri & Bertout 1989; Bouvier 1990), but this object does not exhibit the high-velocity blueshifted absorption predicted by this model. It should be recognized that determinations of inclination angles for individual T Tauri stars are subject to substantial uncertainty.

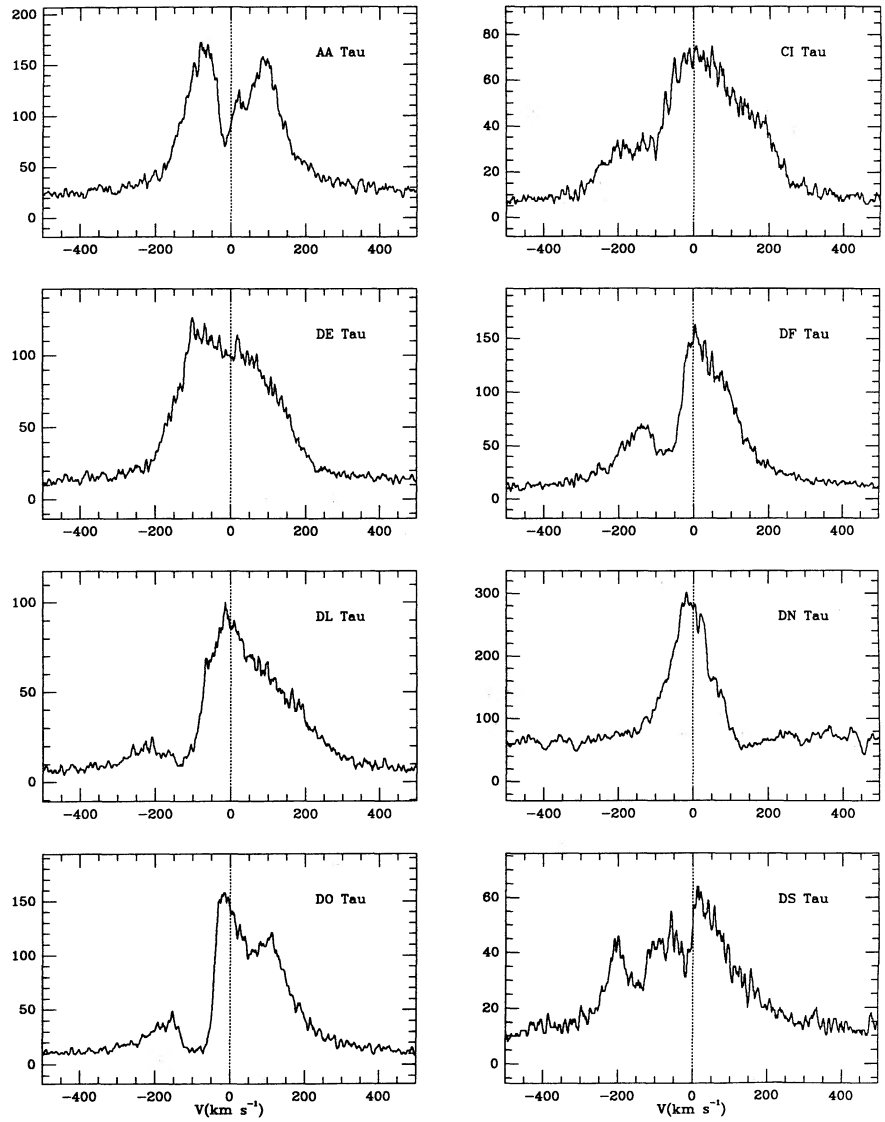

FIG. 6.—Hα line profiles of T Tauri stars, obtained with the FLWO 1.5 m echelle spectrograph and intensified Reticon detector on JD 2446040 and 2446041. The data have been smoothed over the resolution of approximately 12 km s^{-1}. Further details of the instrumentation are given by Latham (1982).

The turbulent wind model profiles do not match the general "triangular" shape of the Hα emission profile, where the emission peaks quite near line center (for example, CI, DF, DL, DN, and DO Tau in Fig. 6). Our observations indicate that half or more of all T Tauri stars have Hα profiles with emission peaks less than 50 km s^{-1} within line center. In contrast, the wind models have emission peaks considerably redward of line center unless observed nearly pole-on or equator-on. The case of polar viewing is statistically unlikely. The high-inclination model profiles are quite flat-topped on the red side of the line, unlike the observed profiles.

This difficulty with getting centrally peaked line profiles or triangular-shaped emission profiles in our standard wind model arises because of the large turbulent velocities assumed. Profiles with more centrally peaked emission can be produced by reducing the turbulent velocity. However, reducing v_{turb} results in line shapes much more like the classical P Cygni profile, with the blue side of the line dominated by absorption (Fig. 2, *leftmost panels*), and this type of profile is not typically observed.

Another problem with accelerating wind models is the general prediction of high-velocity blueshifted absorption in the Hβ and Hγ lines. There is a lack of simultaneous Balmer line profile observations in the literature, but the data of Basri et al. (1989) suggest that the Hβ and Hγ line profiles of many T Tauri stars are more symmetric than the Hα profiles. Many Hβ and Hγ observations show no evidence for absorption reversals. Such absorption reversals are very difficult to avoid in the wind models. Large Hα emission equivalent widths and large Hα to Hβ ratios require large optical depths in the Balmer lines in these models (see Hartmann et al. 1990). With such large optical depths [$\tau(H\alpha) \sim 10^3$], non–LTE effects generally produce blueshifted absorption reversals in the first three members of the Balmer series.

In summary, it appears that turbulent wind models have difficulty in explaining the observed line profiles of many T

Tauri stars. The adoption of large turbulent velocity makes it difficult to obtain centrally peaked emission line profiles. Adopting a cone geometry for the flow helps move the central absorption reversal near line center, in better agreement with observations, but even with cone outflow the blueshifted absorption is generally too strong in the higher Balmer lines.

Although we have explored very little of parameter space for rotating wind models, rapid rotation does not appear to help in matching the observed emission line profiles. Rotation produces double-peaked profiles which are relatively rare in strong-emission T Tauri stars. Another problem is the magnitude of the expected rotational velocity. The Keplerian velocity of the inner disk is $v_K = 275(M/0.8\ M_\odot)^{0.5}(R/2\ R_\odot)^{-0.5}$. For the model calculations presented in Figure 5 we have assumed an inner disk rotation velocity of only 200 km s^{-1}, but even with a modest Alfvén radius of only $2.5R_*$ the edge of the red emission wing of Hα is at $\sim +300$ km s^{-1} when the star is observed at a typical inclination of 60°, and this is a relatively large velocity width compared to observations.

To examine the constraints on rotating wind models more carefully, Hα line widths were measured for our sample of 31 T Tauri stars. The width of the line was defined to be the velocity at which the long-wavelength side of the Hα emission declines to 25% of its peak value. Only the red side of the line is used in order to avoid the skewing effects of blueshifted wind absorption.

Figure 7 demonstrates that most T Tauri stars have emission wings which extend to redshifted velocities less than 250 km s^{-1} from line center. The Hα line width of our rotating wind model is clearly too large when viewed at inclinations $\gtrsim 60°$. This problem could be alleviated if the Hα is optically thin in the most rapidly rotating regions of the envelope, but this would decrease the line equivalent width, which is already too small. The rotational broadening would be smaller if corotation is enforced only out to a radius less than $2R_*$, but then it is difficult to accelerate the wind to escape velocities. The problem of excessive rotational velocity broadening might be eliminated if much of the wind arises from outer, more slowly rotating disk regions (Königl 1989).

It must be emphasized that the above discussion *assumes* that the observed emission is produced in the expanding regions of the flow. If the emission actually arises in the infalling envelope, as we suggest in a companion paper (Calvet & Hartmann 1991), then obviously emission line widths cannot be used to constrain outflow velocity fields.

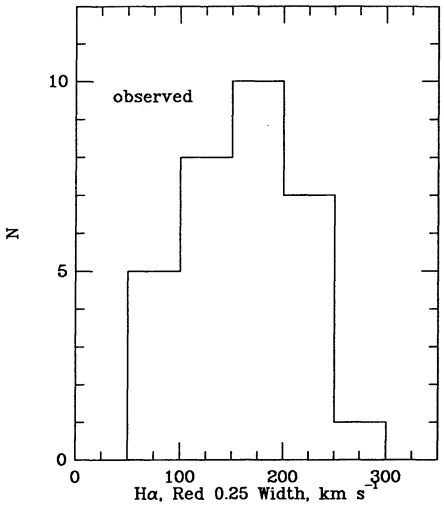

FIG. 7.—Observed Hα line widths for 31 T Tauri stars. The width is defined to be the velocity redward of line center where the emission line decreases to 0.25 of its peak value.

5. CONCLUSIONS

We have computed Balmer line profiles for a class of T Tauri wind models in which the flow originates from the inner disk. Turbulent wind models with cone geometry exhibit blueshifted absorption with lower velocities, in better agreement with observations. However, the calculated profiles are not very successful in explaining the centrally peaked emission observed in many T Tauri stars, and the models also tend to predict too much blueshifted absorption in Hβ and Hγ. Thus, a cone wind geometry does not adequately explain the Balmer line observations of many objects. Rapid rotation does not improve the agreement between theory and observations. The resulting emission line wings are too broad if the flow originates in the innermost disk regions, rotating at the local Keplerian velocity.

It is obviously difficult to draw definite conclusions in the absence of predictions for detailed hydrodynamic and thermodynamic wind calculations. We have necessarily investigated only a small fraction of the parameter space available to empirical models. However, it is significant that many wind models have difficulties in explaining the observed line profiles.

We are indebted to Gibor Basri for providing us with his observations of T Tauri stars for comparison with our models. We gratefully acknowledge many useful comments by Suzan Edwards on the manuscript. Geoge Nassiopoulos drew Figure 1, and was very helpful in transferring data. This work was supported by the International Exchange Program of the Smithsonian Institution and by NASA grant NAGW-511.

REFERENCES

Avrett, E. H., & Loeser, R. 1984, in Methods in Radiative Transfer, ed. W. Kalkofen (Cambridge: Cambridge Univ. Press), 341
Basri, G. B., Rumph, T. F., Batalha, C. C., & Stout, N. M. 1989, BAAS, 21, 716
Basri, G., & Bertout, C. 1989, ApJ, 341, 340
Bertout, C. 1987, in IAU Symp. 122, Circumstellar Matter, ed. I. Appenzeller & C. Jordan (Dordrecht: Reidel), 23
Bertout, C., Basri, G., & Bouvier, J. 1988, ApJ, 330, 350
Blandford, R. D., & Payne, D. G. 1982, MNRAS, 199, 883
Bouvier, J. 1990, AJ, 99, 946
Bouvier, J., Bertout, C., Benz, W., & Mayor, M. 1986, A&A, 165, 110
Cabrit, S., Edwards, S., Strom, S. E., & Strom, K. M. 1990, ApJ, 354, 687
Calvet, N., & Albarrán, J. 1984, Rev. Mexicana Astron. Af., 9, 35
Calvet, N., & Hartmann, L. 1992, ApJ, 386, 239
Camenzind, M. 1990, Reviews in Modern Astronomy, Vol. 3 (Berlin: Springer), in press
Capriotti, E. R. 1965, ApJ, 142, 1101
Castor, J. R. 1970, MNRAS, 149, 111
Cohen, M., Emerson, J. P., & Beichman, C. A. 1989, ApJ, 339, 455
DeCampli, W. M. 1981, ApJ, 244, 124
Edwards, S., Cabrit, S., Strom, S. E., Heyer, I., Strom, K. M., & Anderson, E. 1987, ApJ, 321, 473
Grinin, V. P., & Mitskevich, A. S. 1991, preprint
Hartigan, P., Hartmann, L., Kenyon, S. J., Strom, S. E., & Skrutskie, M. F. 1990, ApJ, 354, L25
Hartmann, L. 1986, Fund. Cosmic Phys., 11, 279
Hartmann, L., Calvet, N., Avrett, E. H., & Loeser, R. 1990, ApJ, 349, 168
Hartmann, L., Edwards, S., & Avrett, E. H. 1982, ApJ, 261, 279
Hartmann, L., Hewett, R., Stahler, S., & Mathieu, R. D. 1986, ApJ, 309, 275
Hartmann, L., & MacGregor, K. B. 1982, ApJ, 257, 264
Herbig, G. H. 1977, ApJ, 214, 747

Holzer, T. E., Fla, T., & Leer, E. 1983, ApJ, 275, 808
Kenyon, S. J., & Hartmann, L. 1987, ApJ, 323, 714
Königl, A. 1989, ApJ, 342, 208
———. 1991, ApJ, 370, L39
Kuan, P. 1975, ApJ, 202, 425
Kuhi, L. V. 1964, ApJ, 140, 1409
Lago, M. T. V. T. 1979, Ph.D. thesis, Univ. Sussex
———. 1984, MNRAS, 210, 323
Latham, D. W. 1982, in IAU Colloq. 67, Instrumentation for Astronomy with Large Optical Telescopes, ed. C. M. Humphries (Dordrecht: Reidel), 259
Lynden-Bell, D., & Pringle, J. E. 1974, MNRAS, 168, 303
Mihalas, D. 1978, Stellar Atmospheres (San Francisco: Freeman)
Natta, A., & Giovanardi, C. 1990, ApJ, 356, 646
Natta, A., Giovanardi, C., & Palla, F. 1988, ApJ, 332, 921
Pringle, J. E. 1989, MNRAS, 236, 107
Pudritz, R. E., & Norman, C. A. 1983, ApJ, 274, 677